



Optimization of electron transmission on a 1D lattice

Walter Unglaub^a, A.F.J. Levi^{a,b,*}

^a Department of Electrical and Computer Engineering, University of Southern California, Los Angeles, CA, 90089-2533, USA

^b Department of Physics and Astronomy, University of Southern California, Los Angeles, CA, 90089-2533, USA

ARTICLE INFO

Editor: Horacio Pastawski

Keywords:

Optimization of heterostructure potential profile
Electron transmission
Tunnel diode
Complex band structure
Tight-binding approximation

ABSTRACT

Finding optimal multi-layer heterostructure configurations that result in desired current–voltage characteristics requires physical control of electron scattering processes. It is shown how a one-dimensional tight-binding Hamiltonian combined with the adjoint method may be employed to explore this non-convex and non-intuitive design space. Such optimal parameter exploration has application to study of vertical electron transport through van der Waals stacked few-layer quantum materials and nano-scale single-crystal semiconductor heterostructures.

1. Introduction

Vertical electron transport through few-layer stacks of quantum materials is of both fundamental and practical interest. For example, the application of resonant tunneling with vertical electron transport through van der Waals stacked few-layer heterostructures has been demonstrated recently [1]. It has also been shown that twist angle in stacked black phosphorus homostructures can have the current–voltage characteristic of a resonant tunnel diode [2]. These and other studies [3–10] indicate an opportunity for creation of few-layer stacks of quantum materials with electronic properties that can be tuned for function. Given the extraordinarily large number of design choices available, it seems appropriate to consider using numerical search methods to assist in the discovery of optimal combinations of materials and geometries for desired functionalities.

Previous studies have shown that atomic layer precision available in the creation of single-crystal semiconductor heterostructure tunnel diodes can be used to design a specific current–voltage characteristic over a range of voltage bias [11]. In the case of the $\text{Al}_\xi\text{Ga}_{1-\xi}\text{As}$ material system, a number of tunnel barriers of uniform thickness can have different tunnel barrier energies by varying alloy fraction, ξ . The optimal device design methodology used provides one-dimensional (1D) semiconductor conduction band profiles that, while non-intuitive, are robust against small variations in individual heterostructure tunnel barrier potential and thickness.

This approach to discovery utilizes a forward physical model with an effective electron mass approximation to describe conduction band electrons and tunneling. However, the use of effective electron mass

$m_e^* = m_{\text{eff}} \times m_0$, where m_0 is the bare electron mass, limits accessibility to objective current–voltage characteristics. This deficiency is addressed here by adopting a more general tight-binding Hamiltonian that was originally developed to approximate the wave functions of electrons in a crystalline solid using linear combinations of atomic orbitals [12].

Initial studies using the tight-binding model of electronic structure considered nearest-neighbor interactions with an emphasis on symmetry [13], complex band structure [14–16], as well as computationally efficient calculations for the electronic properties of crystalline solids [17,18]. The tight-binding model has also been extensively used to explore band structure in one-, two-, and three-dimensional systems [19–23] and Green's function methods have been used to study electron transport in a variety of lattice topologies described by nearest-neighbor and next-nearest-neighbor tight-binding models with different boundary conditions [24–32]. Recent work has also generalized Bloch's theorem used in tight-binding Hamiltonians for arbitrary boundary conditions [33,34].

In the results presented here, accessibility to a wide range of objective current–voltage characteristics in few-layer quantum heterostructures described by a 1D tight-binding Hamiltonian is explored by solving for electron transport with a Green's function method, using the adjoint method to calculate gradients with respect to experimentally accessible parameters [35], and implementing efficient search for globally optimal configurations. The solution space for electron scattering on a lattice with onsite potential values that vary as a function of position is very large and often challenging to interpret. However, as with specific non-optimized configurations [36], the dispersion relation associated

* Corresponding author at: Department of Electrical and Computer Engineering, University of Southern California, Los Angeles, CA, 90089-2533, USA.
E-mail address: alevi@usc.edu (A.F.J. Levi).

<https://doi.org/10.1016/j.physe.2024.116067>

Received 16 March 2024; Received in revised form 31 July 2024; Accepted 12 August 2024

Available online 14 August 2024

1386-9477/© 2024 The Author(s). Published by Elsevier B.V. This is an open access article under the CC BY license (<http://creativecommons.org/licenses/by/4.0/>).

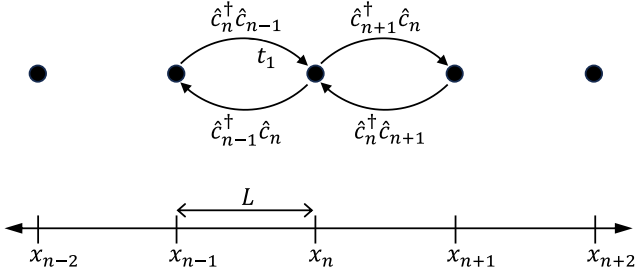


Fig. 1. Atom positions for a 1D lattice with nearest-neighbor spacing L . Nearest-neighbor electron hopping energy to or from the n th atomic site located at position x_n is t_1 . The electron creation and annihilation operators at the n th site are \hat{c}_n^\dagger and \hat{c}_n , respectively.

with *bulk* complex band structure can guide and contribute to understanding material properties that provide accessibility to objective characteristics of interest for nano-scale electronic device applications.

2. Tight-binding model and complex band structure

Optimal design can benefit from an efficient forward physical model that captures the essential physics of vertical electron transport in single-crystal and van der Waals heterostructures. Key elements of the simplest such physical model might include a tight-binding approximation and employ a Green's function approach to calculate the transmission of an electron on a 1D lattice.

2.1. Hamiltonian and dispersion relation

The domain of the 1D lattice being considered is illustrated in Fig. 1 and consists of N_{at} sites, each with a single atomic s-orbital, nearest-neighbor hopping energy t_1 , and lattice spacing L . Nearest-neighbor electron hopping occurs via creation (\hat{c}_n^\dagger) and annihilation (\hat{c}_n) operators at the n th site, with $|0\rangle$ denoting the vacuum state such that $\hat{c}_n|0\rangle = 0$ and $\hat{c}_n^\dagger|0\rangle = |n\rangle$ corresponding to a single electron occupying the lattice site at position $x_n = nL$. The total potential energy $\hat{V} = \hat{U} + \hat{V}_{\text{bias}} + \hat{E}_0$ of the system is the sum of N_{at} real onsite values $\hat{U} = U(x_n)\hat{c}_n^\dagger\hat{c}_n$, the applied bias potential $\hat{V}_{\text{bias}} = eV_{\text{bias}}(x_n)\hat{c}_n^\dagger\hat{c}_n$, and reference energy $\hat{E}_0 = E_0(x_n)\hat{c}_n^\dagger\hat{c}_n$, such that $V_n = U(x_n) + V_{\text{bias}}(x_n) + E_0(x_n)$. Hence, before introducing an electron source term, the Hamiltonian for nearest-neighbor hopping is

$$\hat{H} = \sum_{n=1}^{N_{\text{at}}} V_n \hat{c}_n^\dagger \hat{c}_n - t_1 \sum_{n=1}^{N_{\text{at}}} (\hat{c}_n^\dagger \hat{c}_{n+1} + \hat{c}_{n+1}^\dagger \hat{c}_n) \quad (1)$$

or, expressed as a tri-diagonal matrix,

$$\hat{H} = \begin{bmatrix} V_1 & -t_1 & 0 & \cdots & 0 \\ -t_1 & V_2 & -t_1 & \cdots & 0 \\ 0 & -t_1 & V_3 & \cdots & 0 \\ \vdots & \vdots & \vdots & \ddots & -t_1 \\ 0 & 0 & 0 & -t_1 & V_{N_{\text{at}}} \end{bmatrix}. \quad (2)$$

If $U(x_n) = V_{\text{bias}}(x_n) = 0$ and $E_0(x_n) = E_0$ then the Bloch wave function is $\psi_{n\pm 1} = \psi_n e^{\pm ikL}$ and an electron of energy $E = \hbar\omega(k)$ with Bloch wave vector k satisfies

$$E\psi_n = E_0\psi_n - t_1 (e^{ikL} + e^{-ikL}) \psi_n. \quad (3)$$

Setting reference energy $E_0 = 2t_1$ and $N_{\text{at}} \rightarrow \infty$, the nearest-neighbor electron energy dispersion relation for pure real values of k is

$$E = 2t_1(1 - \cos(kL)) \quad (4)$$

where it follows that

$$kL = \cos^{-1} \left(1 - \frac{E}{2t_1} \right). \quad (5)$$

Eq. (5) gives rise to complex band structure with pure-real values of kL corresponding to delocalized propagating states when $0 < E < 4t_1$ relative to the bottom of the conduction band and complex values of kL corresponding to non-propagating states that exist in the complex plane when $E < 0$ and $E > 4t_1$. Any complex value of kL is not a proper solution to Schrödinger's equation for one electron in a periodic potential because it violates translational invariance in the lattice and the wave function grows exponentially (unbounded) in space. Delocalized non-propagating states with energies at band extrema connect pure real and complex solutions (which, in this case, occurs when $E = 0$ and $E = 4t_1$).

2.2. Next-nearest-neighbor hopping

Inclusion of a next-nearest-neighbor hopping energy term, t_2 , modifies the Hamiltonian matrix (Eq. (2)) to

$$\hat{H} = \begin{bmatrix} V_1 & -t_1 & -t_2 & 0 & \cdots & \cdots & 0 \\ -t_1 & V_2 & -t_1 & -t_2 & & & \vdots \\ -t_2 & -t_1 & V_3 & -t_1 & \ddots & & \vdots \\ 0 & -t_2 & -t_1 & V_4 & \ddots & & \vdots \\ \vdots & & \ddots & \ddots & \ddots & -t_1 & -t_2 \\ \vdots & & & \ddots & -t_1 & V_{N_{\text{at}}-1} & -t_1 \\ 0 & \cdots & \cdots & \cdots & -t_2 & -t_1 & V_{N_{\text{at}}} \end{bmatrix} \quad (6)$$

and Eq. (4) becomes

$$E = 2(t_1 + t_2) - 2t_1 \cos(kL) - 2t_2 \cos(2kL). \quad (7)$$

This can introduce additional structure in both the dispersion of propagating states with pure-real values of k and non-propagating states with complex values of k .

2.3. Boundary conditions

An impulse source at the far left lattice site position $x_s = x_1$ may be written as a vector $\mathbf{s} \equiv s_n \delta(x_n - x_1)$. This is included in the nearest-neighbor Hamiltonian as source and sink terms at the respective left and right boundaries of the domain such that

$$\hat{H}' \equiv \hat{H} - \hat{B}. \quad (8)$$

The boundary term \hat{B} is zero everywhere except at the onsite boundary elements B_1 and $B_{N_{\text{at}}}$ such that in matrix form

$$\hat{B} = \begin{bmatrix} B_1 & 0 & \cdots & \cdots & 0 \\ 0 & 0 & & & \vdots \\ \vdots & & \ddots & & \vdots \\ \vdots & & & 0 & 0 \\ 0 & \cdots & \cdots & 0 & B_{N_{\text{at}}} \end{bmatrix}. \quad (9)$$

At position x_L sufficiently far to the left of the region containing the scattering potential, the wave function describing electron motion in a constant potential may be written as the sum of incident and reflected terms

$$\psi_n = A e^{ikx_n} + B e^{-ikx_n}, \quad (10)$$

where A and B are the amplitude coefficients of the incident and reflected waves, respectively. Setting $A = 1$, a source to the left of the n th atomic site near the left boundary, $x_L = (n-1)L$ has wave function

$$\begin{aligned} \psi_{n-1} &= e^{ik(n-1)L} + B e^{-ik(n-1)L} \\ &= e^{iknL} e^{-ikL} + B e^{-iknL} e^{ikL} + (e^{ikL} - e^{-ikL}) e^{iknL} \\ &= (e^{iknL} + B e^{-iknL}) e^{ikL} + (e^{-ikL} - e^{ikL}) e^{iknL} \\ &= \psi_n e^{ikL} - 2i \sin(kL) e^{iknL}. \end{aligned} \quad (11)$$

The corresponding nearest-neighbor Hamiltonian matrix element value B_1 for the left boundary condition is found by substituting Eq. (11) for the left edge, ψ_{n-1} , into the Schrödinger equation,

$$\hat{H}'_n \psi_n = V_n \psi_n - t_1 \psi_{n+1} - t_1 \psi_{n-1} = E \psi_n, \quad (12)$$

so that

$$(V_n - E) \psi_n - t_1 \psi_{n+1} - t_1 (\psi_n e^{ikL} - 2i \sin(kL) e^{iknL}) = 0 \quad (13)$$

and

$$\begin{aligned} (V_n - t_1 e^{ikL} - E) \psi_n - t_1 \psi_{n+1} = \\ (\hat{H}'_n - E) \psi_n = \hat{H}_n \psi_n = -2t_1 i \sin(kL) e^{iknL}. \end{aligned} \quad (14)$$

Hence,

$$B_1 = t_1 e^{ikL} \quad (15)$$

and the far left source term is

$$s_1 = -2t_1 i \sin(kL) e^{ikx_1}. \quad (16)$$

Similarly, at the far right position x_R , the wave function describing electron motion in a constant potential with transmission and reflection coefficients C and D , respectively, is

$$\psi_n = C e^{ikx_n} + D e^{-ikx_n} \quad (17)$$

and, for open boundary conditions and no source on the right-hand-side, $D = 0$. The wave function located to the right of the n th atomic site near the right boundary at position $x_R = (n+1)L$ may be written as

$$\psi_{n+1} = C e^{ik(n+1)L} = (C e^{iknL}) e^{ikL} = \psi_n e^{ikL}. \quad (18)$$

Substituting Eq. (18) into the Schrödinger equation (Eq. (12)) gives

$$(V_n - E) \psi_n - t_1 (\psi_n e^{ikL}) - t_1 \psi_{n-1} = 0 \quad (19)$$

and so

$$\begin{aligned} (V_n - t_1 e^{ikL} - E) \psi_n - t_1 \psi_{n-1} = \\ (\hat{H}'_n - E) \psi_n = \hat{H}_n \psi_n = 0. \end{aligned} \quad (20)$$

Just as with the left boundary, the corner diagonal element of the nearest-neighbor Hamiltonian corresponding to the right boundary introduces the term

$$B_{N_{\text{at}}} = t_1 e^{ikL}. \quad (21)$$

However, since the source is taken to be incident from the left boundary, the right boundary element of the source vector is $s_{N_{\text{at}}} = 0$.

Electron phase, $\phi = kL$, is calculated at the boundaries by accounting for the energy difference between the electron energy, E , and total onsite potential energy, V_n , for $n = 1$ at the left boundary and $n = N_{\text{at}}$ at the right boundary. From the dispersion relation given by Eq. (3), $E = V_n - 2t_1 \cos(\phi_n)$, and the phase at the n th site is

$$\phi_n = \cos^{-1} \left(\frac{V_n - E}{2t_1} \right). \quad (22)$$

2.4. Green's function solution

A linear operator $\hat{H} = \hat{H}' - E\hat{1}$ which accounts for boundary conditions and the total electron energy E may be constructed so that

$$\begin{aligned} \hat{H}\psi &= E\psi + (s + \hat{B}\psi) \\ (\hat{H} - \hat{B})\psi &= \hat{H}'\psi = E\psi + s \\ (\hat{H}' - E\hat{1})\psi &= \hat{H}\psi = s. \end{aligned} \quad (23)$$

In matrix form, $\hat{H}\psi = s$ may be written as

$$\begin{bmatrix} H_1 & -t_1 & \cdots & \cdots & 0 \\ -t_1 & H_2 & \ddots & & \vdots \\ \vdots & \ddots & \ddots & \ddots & \vdots \\ \vdots & & & H_{N_{\text{at}}-1} & -t_1 \\ 0 & \cdots & \cdots & -t_1 & H_{N_{\text{at}}} \end{bmatrix} \begin{bmatrix} \psi_1 \\ \psi_2 \\ \vdots \\ \psi_{N_{\text{at}}-1} \\ \psi_{N_{\text{at}}} \end{bmatrix} = \begin{bmatrix} s_1 \\ s_2 \\ \vdots \\ s_{N_{\text{at}}-1} \\ s_{N_{\text{at}}} \end{bmatrix}, \quad (24)$$

where the elements $H_1 = V_1 - E - B_1$ and $H_{N_{\text{at}}} = V_{N_{\text{at}}} - E - B_{N_{\text{at}}}$ at the respective left and right boundaries, and $H_n = V_n - E$ at all other sites. Thus, computing the electron wave function is equivalent to solving

this matrix equation for ψ by inverting the matrix \hat{H} and multiplying both sides by the Green's function $G = \hat{H}^{-1}$ so that

$$\begin{aligned} \hat{H}\psi &= s \\ \hat{H}^{-1}\hat{H}\psi &= \hat{H}^{-1}s \\ \psi &= Gs. \end{aligned} \quad (25)$$

If there is a single source term at the left boundary position x_1 , then source element s_1 is the only nonzero entry in the vector s .

3. The resonant tunnel diode

The current-voltage characteristic of a conventional symmetric two-barrier resonant tunnel diode with conduction band minimum profile illustrated in the inset of Fig. 2(a) can be modeled in the depletion approximation using the tight-binding formalism. The left and right hand tunnel barriers sketched in the inset have potential energies V_{B1} and V_{B2} respectively with $V_{B1} = V_{B2}$.

Fig. 2(a) shows results of calculating current density, J , as a function of applied voltage bias, V_{bias} , using parameters corresponding to those for the AlGaAs material system. Carrier density in the GaAs electrodes is $n_0 = 10^{18} \text{ cm}^{-3}$, each undoped AlGaAs barrier consists of 10 lattice sites with each site having the same onsite potential energy 0.30 eV, each barrier has thickness $L_B = 2.83 \text{ nm}$, and well thickness is $L_W = 4.52 \text{ nm}$. Temperature $T = 300 \text{ K}$ and the chemical potential deep in the electrodes is $\mu = 38.9 \text{ meV}$. The results shown in Fig. 2(a) agree with those previously published using an effective mass approximation [37]. The peak-to-valley current ratio is $\text{PVR} = 6.1$ with peak current occurring at $V_{\text{bias,peak}} = 0.145 \text{ V}$ and valley current occurring at $V_{\text{bias,valley}} = 0.264 \text{ V}$.

Even though the Schrödinger equation is solved for a finite-sized nano-scale structure, it is helpful to refer to states in the bulk band structure for which $N_{\text{at}} \rightarrow \infty$ [38]. Fig. 2(b) illustrates the corresponding bulk complex band structure states accessed by an electron of energy $E_{\text{el}} = 0.05 \text{ eV}$ incident on the potential profile from the left of the system when $V_{\text{bias}} = 0$.

Achieving a high peak current, small negative differential resistance, and high PVR can be of practical interest. To this end, it is advantageous to be guided by access to different states of the complex band structure described by the next-nearest-neighbor dispersion relation. This consideration suggests modifying the second barrier by shifting the energy by $\Delta E = 4t_1$ so that $V_{B2} = V_{B1} - \Delta E$. Doing so results in a comparable peak current value with a substantially higher PVR. See Fig. 3(a).

Fig. 3(b) illustrates how an incoming electron of energy $E_{\text{el}} = 0.05 \text{ eV}$ may be viewed as accessing states in the band structure with large value of k and that this can result in a larger PVR. Increasing the number of potential barriers used and adopting an optimal design methodology is expected to increase the number of resonant states and provide a path to further improvement of PVR. This approach is considered next.

4. Application to optimal design

An optimal design problem with \mathcal{P} experimentally-accessible, continuously-variable bounded design parameters typically employs a cost function to measure the distance between an objective and a simulation. In this problem the n th layer of the heterostructure device has thickness L_n and onsite potential U_n . The values of these design parameters are placed into a vector \mathbf{p} containing \mathcal{P} entries. A scalar measure of optimality is

$$C_{\text{cost}}(\mathbf{p}) = \sum_{j=1}^{N_{\text{bias}}} w_j |J_{\text{obj}}(V_{\text{bias},j}) - J_{\text{sim}}(V_{\text{bias},j}, \mathbf{p})|^r \quad (26)$$

in which the objective is the current density function $J_{\text{obj}}(V_{\text{bias}})$ and the simulated current density $J_{\text{sim}}(V_{\text{bias}}, \mathbf{p})$ is the output of the forward physical model for feasible input design parameter values \mathbf{p} . The discrete

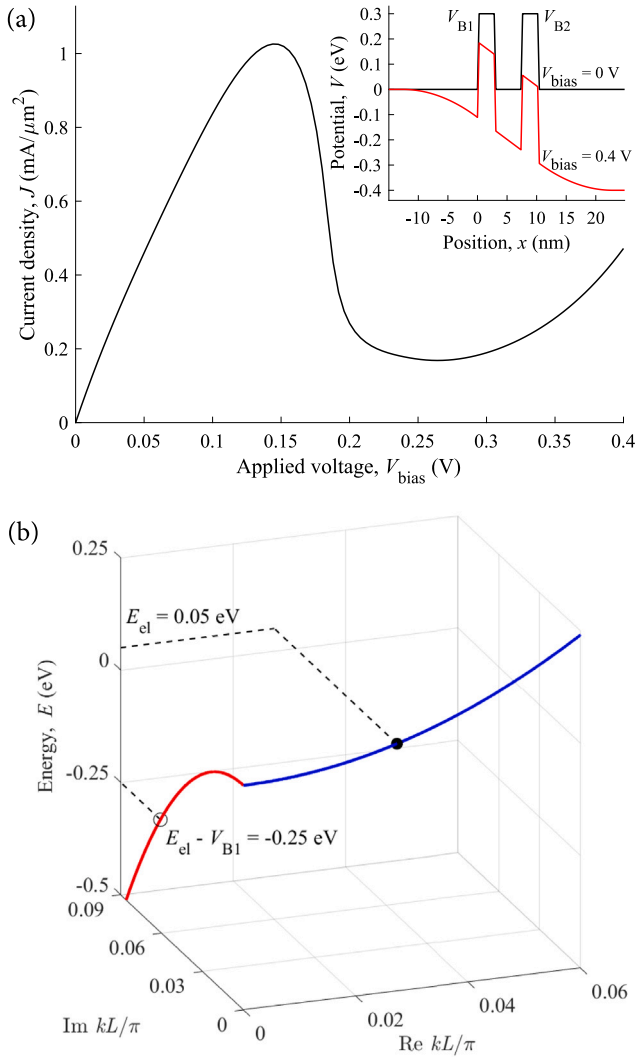


Fig. 2. (a) Current–voltage characteristic of the double barrier resonant tunnel diode structure shown in the inset without a bias voltage (black) and with bias voltage $V_{\text{bias}} = 0.4$ V (red). $J_{\text{peak}} = 1.03$ mA/μm² and PVR = 6.1. Parameters: $T = 300$ K, $n_0 = 10^{18}$ cm⁻³, $L = 0.283$ nm, $V_{B1} = V_{B2} = 0.30$ eV, $L_B = 2.83$ nm, $L_W = 4.52$ nm, $x_s = -15$ nm, $x_R = 24.9$ nm, $m_{\text{eff}} = 0.07$, $t_1 = 6.81$ eV. (b) Nearest-neighbor tight-binding complex band structure with reference energy $E_0 = 2t_1$, has propagating electron states with pure-real k (blue curve) and non-propagating electron states with complex k (red curve). An incoming electron with energy $E_{\text{el}} = 0.05$ eV is represented by the black dot on the pure-real band and the open circle on the pure-imaginary band is associated with a tunneling state.

sum over N_{bias} sample points in Eq. (26) is necessary for numerical evaluation. For the case being considered, a uniform weight factor $w_j = 1$ is applied and the distance is chosen to be an L^2 measure of the difference between the simulated current density, J_{sim} , and the objective function, J_{obj} , so that $\gamma = 2$.

Sufficient conditions to ensure a locally optimal device configuration, \mathbf{p}^* , in the minimization problem,

$$\min_{\mathbf{p}} C_{\text{cost}}, \quad (27)$$

are

$$\nabla_{\mathbf{p}} C_{\text{cost}}|_{\mathbf{p}^*} = 0 \quad (28)$$

and

$$\mathbf{H}_{\mathbf{p}}(C_{\text{cost}})|_{\mathbf{p}^*} > 0, \quad (29)$$

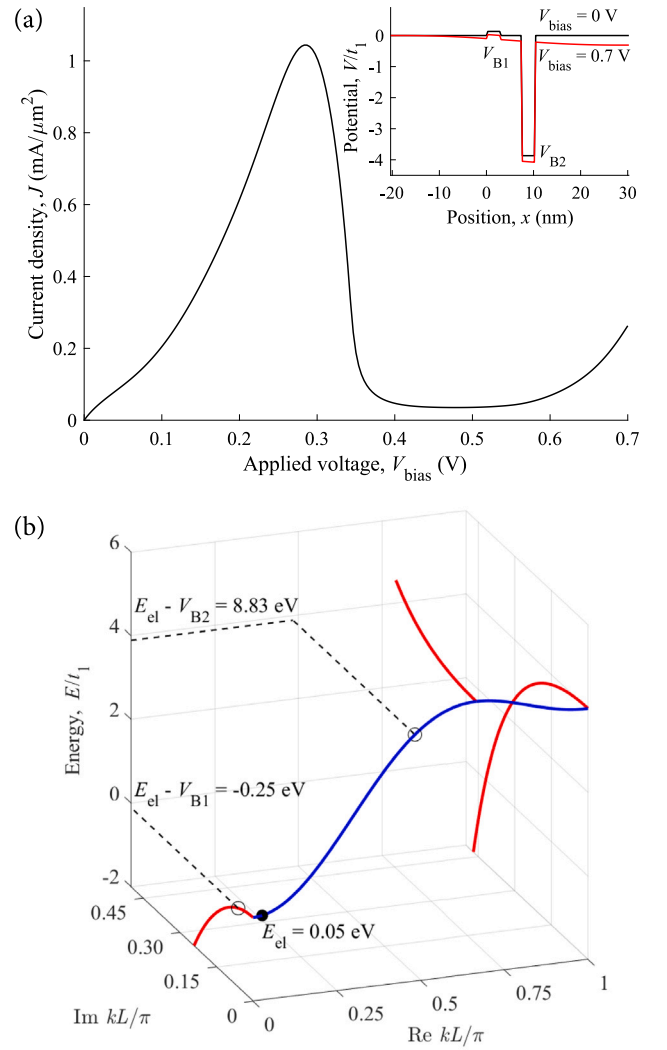


Fig. 3. (a) Current–voltage characteristic of structure with potential profile shown in inset. Barrier potential V_{B2} has energy offset of $\Delta E = 4t_1$. $J_{\text{peak}} = 1.04$ mA/μm² and PVR = 30. (b) Complex band structure using next-nearest-neighbor hopping with $t_2 = 0.5t_1$, and reference energy $E_0 = 2(t_1 + t_2)$. For an incoming electron with energy $E_{\text{el}} = 0.05$ eV represented by the black dot on the pure-real band, the energy offsets from the bottom of the conduction band due to barriers V_{B1} and $V_{B2} = V_{B1} - 4t_1$ are respectively represented by the black open circles on the pure-imaginary and pure-real bands. Parameters: $T = 300$ K, $L = 0.283$ nm, $t_1 = 2.27$ eV, $t_2 = 1.135$ eV, $n_0 = 10^{18}$ cm⁻³, $V_{B1} = 0.30$ eV, $L_B = 2.83$ nm, $L_W = 4.52$ nm, $x_s = -20.4$ nm, $x_R = 30.2$ nm.

where $\mathbf{H}_{\mathbf{p}}$ is the Hessian matrix and the elements in \mathbf{p} belong to the experimentally-accessible design parameter space.

A cost function, such as Eq. (26), can be non-convex. It is this fact and a typically high-dimensional parameter space that can make the minimization problem described by Eq. (27) a challenge. It is possible that both multiple local minima exist and that many solutions exist that have a cost value close to optimal.

The cost function may be minimized using Newton's method by sequentially applying

$$\mathbf{p}_{k+1} = \mathbf{p}_k - \frac{\nabla_{\mathbf{p}} C_{\text{cost}}}{\mathbf{H}_{\mathbf{p}}(C_{\text{cost}})} \quad (30)$$

to approximate $\nabla_{\mathbf{p}} C_{\text{cost}}|_{\mathbf{p}^*} = 0$. This does, of course, require evaluation of $\nabla_{\mathbf{p}} C_{\text{cost}}$.

An efficient way to calculate the P -dimensional gradient $\nabla_{\mathbf{p}} C_{\text{cost}}$ is to use the adjoint method.

4.1. Adjoint method

The adjoint method casts the forward solve in terms of a linear system

$$\mathbf{L}(\mathbf{p}) \cdot \mathbf{t} = \mathbf{b} \quad (31)$$

where the matrix $\mathbf{L}(\mathbf{p})$ incorporates the device physics, vector \mathbf{t} contains the unknown transmitted wave function amplitudes from which $J_{\text{sim},j} = W_j(\mathbf{t})$ is obtained, and vector \mathbf{b} contains the boundary conditions.

The \mathcal{P} -dimensional gradient $\nabla_{\mathbf{p}} C_{\text{cost}}$ may be found using the chain rule. Setting $w_j = 1$ and $\gamma = 2$ in Eq. (26), the derivative of the l th design parameter in C_{cost} may be written

$$\begin{aligned} \partial_{p_l} (C_{\text{cost}}(\mathbf{p})) = \\ - \sum_{j=1}^{N_{\text{bias}}} 2[J_{\text{obj}}(V_{\text{bias},j}) - J_{\text{sim}}(V_{\text{bias},j}, \mathbf{p})] \partial_t W_j(\mathbf{t}) \partial_{p_l} \mathbf{t}, \end{aligned} \quad (32)$$

where, for compactness, $\partial/\partial t = \partial_t$, etc.

The computational expense of approximating the gradient $\nabla_{\mathbf{p}} C_{\text{cost}}$ by \mathcal{P} first-order finite-difference calculations can be avoided by defining an *adjoint equation*

$$\begin{aligned} \mathbf{L}^T(\mathbf{p}) \cdot \mathbf{h} = \\ \sum_{j=1}^{N_{\text{bias}}} 2[J_{\text{obj}}(V_{\text{bias},j}) - J_{\text{sim}}(V_{\text{bias},j}, \mathbf{p})] \partial_t W_j^T(\mathbf{t}). \end{aligned} \quad (33)$$

The adjoint variable \mathbf{h} is found by solving the linear system described by Eq. (33) at the expense of only one forward solve. Making use of the derivative of the forward solve given by Eq. (31),

$$\left(\partial_{p_l} \mathbf{L}(\mathbf{p}) \right) \cdot \mathbf{t} + \mathbf{L}(\mathbf{p}) \cdot (\partial_{p_l} \mathbf{t}) = \partial_{p_l} \mathbf{b}, \quad (34)$$

and substituting Eqs. (33) and (34) into the expression for $\partial_{p_l} (C_{\text{cost}}(\mathbf{p}))$, the derivative of C_{cost} is

$$\partial_{p_l} C_{\text{cost}} = \mathbf{h}^T \cdot \left(\partial_{p_l} \mathbf{L}(\mathbf{p}) \cdot \mathbf{t} - \partial_{p_l} \mathbf{b} \right). \quad (35)$$

It is in this way that the adjoint method avoids the computational burden of evaluating \mathcal{P} additional forward solves that would be required by a finite difference approach to approximating the derivative of C_{cost} . Calculation of the adjoint variable \mathbf{h} has the same computational burden as a single forward solve. Values of \mathbf{t} are calculated during the forward solve and derivatives $\partial_{p_l} \mathbf{L}(\mathbf{p})$ are evaluated analytically.

4.2. Sigmoid current–voltage characteristic

Tight-binding complex band structure as used to describe different materials may be viewed as a guide to improve accessibility to optimal device design when compared with an effective mass model. Specifically, the ability of nearest-neighbor ($t_2 = 0$) and next-nearest-neighbor ($t_2 \neq 0$) models to meet an objective may be explored by applying an optimal design approach. Here, an objective current–voltage characteristic, J_{obj} , is sought by finding an appropriate potential profile composed of N_b barriers, each with barrier thickness $L_b = 4L = 1.132$ nm and onsite potential energy U_n where $n \in \{1, 2, \dots, N_b\}$.

A sigmoid objective function J_{obj} describing a region of negative differential resistance in the current–voltage characteristic of a diode is chosen where

$$J_{\text{obj}}(V_{\text{bias}}) = \frac{J_{\text{max}}}{1 - e^{\nu(V_{\text{bias}} - V_{\text{mid}})}}, \quad (36)$$

in which J_{max} is the asymptotic sigmoid peak, ν is the sigmoid slope parameter, and V_{mid} is the voltage bias value associated with the sigmoid midpoint. For the results presented here, $J_{\text{max}} = 1.055$ mA/ μm^2 , $V_{\text{mid}} = 0.159$ V, and $\nu = 200$ V $^{-1}$.

The difference between the predictions of the forward physical model, J_{sim} , and objective function, J_{obj} , is used to provide a cost function

$$C_{\text{cost}} = \sum_{j=1}^{N_{\text{bias}}} |J_{\text{sim}}(V_{\text{bias},j}) - J_{\text{obj}}(V_{\text{bias},j})|^2, \quad (37)$$

where $J_{\text{obj}}(V_{\text{bias},j}) = J_{\text{obj},j}$ is the objective current density for the j th voltage bias value and $J_{\text{sim}}(V_{\text{bias},j}) = J_{\text{sim},j}$ is the corresponding simulation result from a forward solve measured in units of mA/ μm^2 .

Cost minimization is performed in which the adjoint method provides the gradient, $\partial_{p_l} (C_{\text{cost}}(\mathbf{p}))$, for all N_b variable potential barrier energies to MATLAB's *fmincon* optimization function.

A potential profile with $N_b = 8$ barriers, each of thickness L_b , is studied. To demonstrate the effect of an expanded search space, two sets of bounds on the barrier energies are considered. For the first set, the onsite (barrier) potential energies are restricted to $-0.15 \leq U_n \leq 0.35$ eV which is associated with states near the bottom of a band in, for example, the GaAs/AlInGaAs material system. For the second set, the onsite (barrier) energies are allowed to vary in the range $-4.4 t_1 \leq$

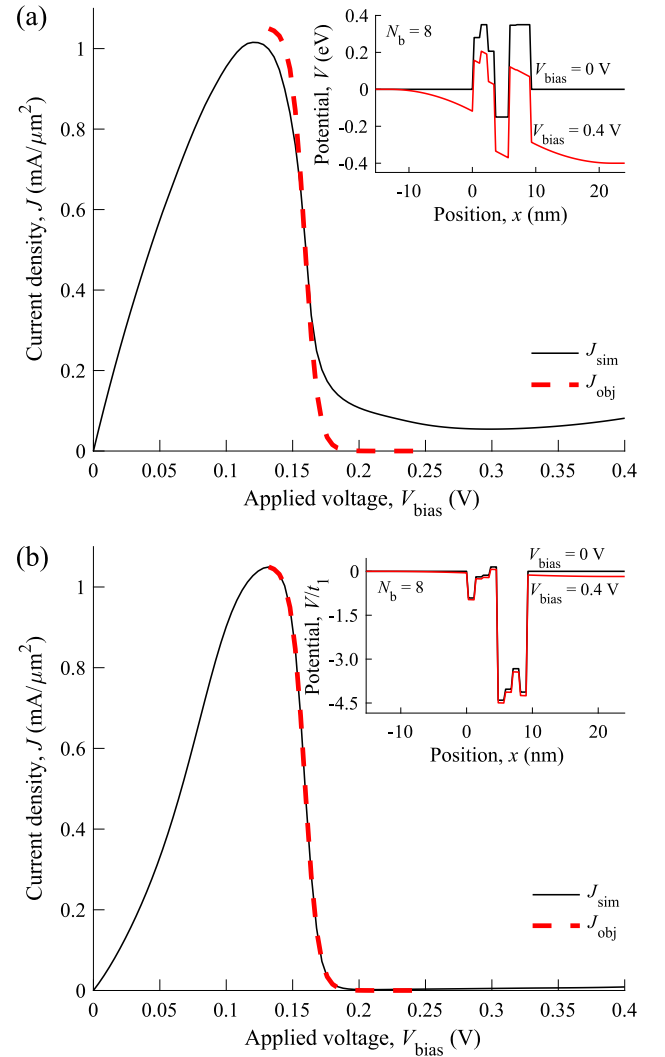


Fig. 4. (a) Sigmoid objective function J_{obj} ($0.132 \text{ V} \leq V_{\text{bias}} \leq 0.252 \text{ V}$) (dashed curve) and optimal result J_{sim} (solid curve). Potential barrier energies $-0.15 \text{ eV} \leq U_n \leq 0.35 \text{ eV}$. Result uses a nearest-neighbor model ($t_2 = 0$) and, other than potential barriers with $L_b = 1.132$ nm and $N_b = 8$, the parameters of Fig. 2. (b) Sigmoid objective function as in (a) and improved optimal result J_{sim} (solid curve). Result uses a next-nearest-neighbor model with $t_1 = 2.27 \text{ eV}$, $t_2 = 0.5 t_1$, $E_0 = 2(t_1 + t_2)$, and potential barrier energies $-4.4 t_1 \leq U_n \leq 0.35 \text{ eV}$. All other parameters are as in (a).

$U_n \leq 0.35$ eV. Initial barrier energies are randomized within the allowed bounded range. To limit computational effort, the maximum number of iterations, n_{iter} , is set to 1000.

Fig. 4(a) shows the best result out of 10 optimization runs using a nearest-neighbor model ($t_2 = 0$) and $-0.15 \leq U_n \leq 0.35$ eV. The peak current is $J_{\text{peak}} = 1.016$ mA/ μm^2 at $V_{\text{bias,peak}} = 0.121$ V and the valley current is $J_{\text{valley}} = 0.054$ mA/ μm^2 at $V_{\text{bias,valley}} = 0.299$ V, yielding PVR = 19 and a negative differential resistance voltage range $\Delta V_{\text{NDR}} = V_{\text{bias,valley}} - V_{\text{bias,peak}} = 0.178$ V. The potential profile is somewhat reminiscent of the conventional symmetric two potential barrier resonant tunnel diode design shown in Fig. 2(a). However, PVR is improved by a factor of approximately 3.

Fig. 4(b) shows the best result out of 10 optimization runs using a next-nearest-neighbor model with $t_2 = 0.5 t_1$ and $-4.4 t_1 \leq U_n \leq 0.35$ eV. The peak current is $J_{\text{peak}} = 1.05$ mA/ μm^2 at $V_{\text{bias,peak}} = 0.132$ V and the valley current is $J_{\text{valley}} = 0.002$ mA/ μm^2 at $V_{\text{bias,valley}} = 0.207$ V, yielding PVR = 509 and a negative differential resistance voltage range $\Delta V_{\text{NDR}} = 0.075$ V. The potential profile is non-intuitive and the improvement in performance is substantial. Compared to the results shown in Fig. 4(a), PVR is improved by a factor of approximately 27 and ΔV_{NDR} is reduced by a factor of almost 2.4.

Another way to illustrate the improvement in performance that is achievable with an increase in resources is to compare convergence of cost, C_{cost} , as a function of iteration number, n_{iter} , for the two cases. Fig. 5 plots convergence of cost for optimization runs with the sigmoid objective function shown in Fig. 4.

Ten optimization runs for the case illustrated in Fig. 4(a) in which $t_2 = 0$ and barrier potential energy is restricted to the range -0.15 eV $\leq U_n \leq 0.35$ eV are shown as black curves. The best result is shown as a black dot. Ten optimization runs for the case illustrated in Fig. 4(b) in which $t_2 = 0.5 t_1$ and $-4.4 t_1 \leq U_n \leq 0.35$ eV are shown as red curves. The best result is shown as a red dot.

The data in Fig. 5 illustrates the fact that access to a larger range of potential barrier energy values is a resource enhancement that the optimization algorithm can exploit to improve convergence of cost by several orders of magnitude.

The computational effort associated with optimization is proportional to iteration number, n_{iter} . Because both cost and n_{iter} in Fig. 5

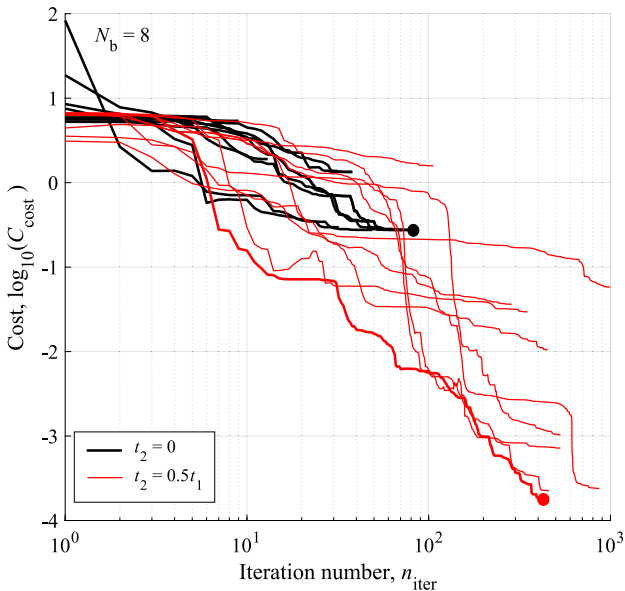


Fig. 5. Convergence of cost as a function of iteration number, n_{iter} , for 10 optimization runs with the sigmoid objective function in Fig. 4, using a nearest-neighbor model where $t_2 = 0$ (black) as well as a next-nearest-neighbor model where $t_2 = 0.5 t_1$ (red) with best run in bold red. Allowing barriers to access a larger energy range improves optimized convergence by more than three orders of magnitude.

are plotted on a logarithmic scale, it is apparent that convergence of the best result tends towards a power-law of the form n_{iter}^α . For the case shown in Fig. 5 the coefficient obtained from a least-squares line-fit of the 10 best solutions out of 100 is $\alpha = -3.1$. The value of α is related to the physical difficulty in achieving the objective for given availability of resources. Resources include the number of layers, bounds to onsite potential value, and access to next-nearest-neighbor hopping ($t_2 \neq 0$). Establishing the value of α in power-law behavior for convergence can contribute to efficiency of search by using it to implement early termination of runs.

5. Discussion

As a first step towards tuning few-layer stacks of quantum materials for specific vertical transport properties, optimization methods are employed to assist in the discovery of non-intuitive potential profiles on a lattice. Electron scattering states in the open system are controlled by tight-binding onsite potentials in the layers. The resulting configurations can have superior functionality compared to those that are the result of (often symmetric) ad-hoc approaches to design.

The physics that the optimization algorithm exploits may be viewed as electron velocity (k -state) mismatch at layer interfaces and the resulting spectrum of broad transmission resonances that vary as a function of applied voltage bias. The interplay between scattering strength and velocity mismatch across different onsite energy values introduces an effective control mechanism for electron transmission behavior through stacked material layers. To gain further insight into this, consider the influence spectral density of electron resonances has on transmission of an electron with energy E_{el} as a function of integer number of atom sites, n_{at} , with uniform onsite potential, U , and $V_{\text{bias}} = 0$.

Fig. 6(a) shows the case when $E_{\text{el}} = 0.05$ eV, integer $1 \leq n_{\text{at}} \leq 40$, -1.7 eV $\leq -U \leq 29$ eV, $L = 0.283$ nm, $t_1 = 6.81$ eV, and $t_2 = 0$. When $U = 0$ there is no electron velocity (k -state) mismatch for any value of n_{at} and electron transmission is unity. As expected, when $U \neq 0$ resonant electron transmission is dependent on the value of U and n_{at} . The spectral position and number of available resonant states in the open system is similar to, but not the same as, the discrete energy eigenvalues of a symmetric tri-diagonal Hamiltonian matrix of Toeplitz form describing an isolated finite lattice of n_{at} sites. Unlike the bound states of the isolated finite lattice, the resonant transmission scattering states have finite spectral linewidth. The number of resonant states increases with n_{at} and, as with the band structure density of states for the cosine dispersion relation of Eq. (4), the spectral density of resonances is concentrated at low and high values of $-U$. However, the resonant transmission spectral linewidth of the open system decreases (and the corresponding quality factor, Q , increases) with increasing $-U$. These higher Q resonances occur as larger-valued k -states of the related band structure are accessed. All resonances are spectrally shifted and broadened as voltage bias, V_{bias} , is applied.

Fig. 6(b) shows electron transmission when $t_1 = 2.27$ eV and $t_2 = 0.5 t_1$. Clearly, the underlying symmetry of Fig. 6(a) is broken. This may be understood in terms of the band structure density of states for the next-nearest-neighbor dispersion relation given by Eq. (7). The increased number of resonances at large values of $-U$ is a useful resource and explains why it is utilized by the algorithm to create the optimal design shown in Fig. 4(b). The introduction of $t_2 \neq 0$ increases resources sufficiently such that configurations with improved performance are accessible (Fig. 4(b)) compared to the case when $t_2 = 0$ (Fig. 4(a)).

Fig. 6(a) and (b) exhibit features that can be traced to the corresponding band structure and it is in this way that bulk complex band structure can be used as a guide to help explain optimal designs of nano-scale structures. In this study each layer is $L_b = 4L$ and there are a total of $N_b = 8$ layers so that $n_{\text{at}} = 32$ and $N_b L_b = 9.0$ nm. The resonances due to electron velocity mismatch at the boundaries of each

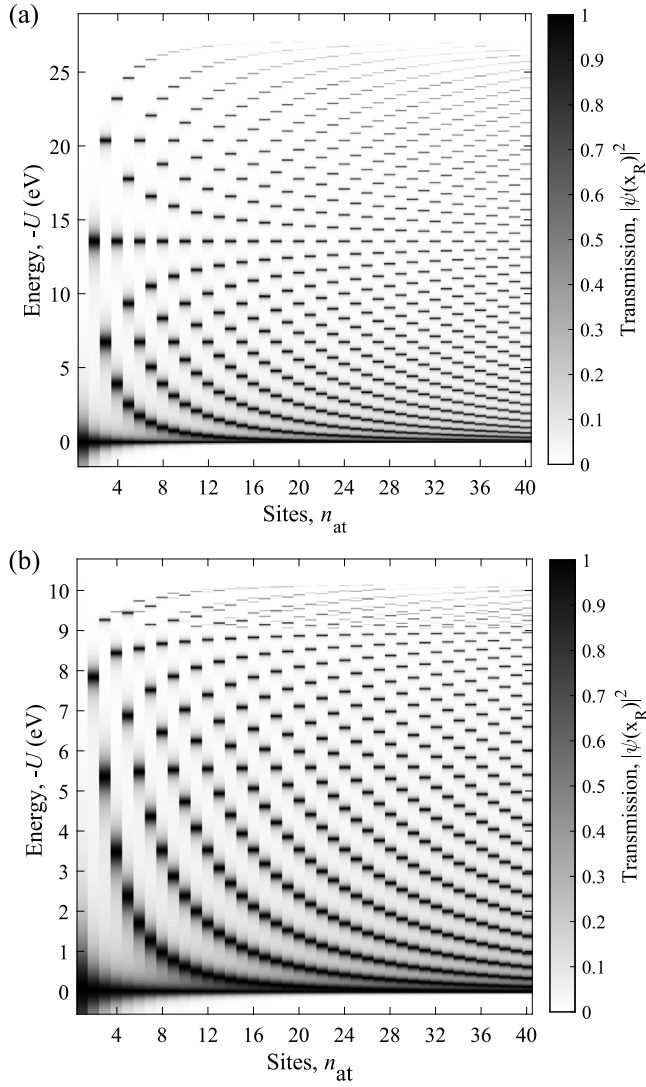


Fig. 6. (a) Transmission of electron with energy $E_{el} = 0.05$ eV for integer $1 \leq n_{at} \leq 40$, -1.7 eV $\leq -U \leq 29$ eV, $L = 0.283$ nm, $t_1 = 6.81$ eV, and $t_2 = 0$. (b) As in (a) except $t_1 = 2.27$ eV, $t_2 = 0.5t_1$, and -0.57 eV $\leq -U \leq 11$ eV.

layer of thickness L_b couple with resonances of other layers and it is this that the algorithm optimizes to meet the objective.

Note that electron tunneling (meaning access to electron states with complex values of k) is *not* necessary to obtain a resonant tunnel diode current–voltage characteristic of the type shown in Fig. 2(a). Current–voltage characteristics can be obtained by varying U to manipulate the spectral position of resonances due to electron velocity mismatch of states that correspond to propagating k -states of the real band structure.

The approach taken in this study has been to use a minimalist forward physical model that can demonstrate improved design optimization when increased resources are provided. As with the epitaxially grown single-crystal AlInGaAs material system, onsite potential, U , is assumed to be a continuous variable. To maintain simplicity, the detailed electronic structure of specific few-layer quantum materials and geometries, including extensions to two- and three-dimensions, has not been explored. The 1D tight-binding Hamiltonian used in this study could be extended to two dimensions by, for example, considering an

$N_{at} \times N_{at}$ square lattice and modifying Eq. (1) to include (n, m) labels for respectively indexing sites along the (x, y) axes in the 2D lattice. This would result in a Hamiltonian matrix of size $N_{at}^2 \times N_{at}^2$ and introduce additional kinetic energy terms to describe electron hopping along the y -direction. Care must then be taken to apply the appropriate boundary conditions such that the Green’s function is correctly calculated from the resulting effective Hamiltonian [25].

Also missing from our approach are complications arising from inelastic electron scattering and self-consistent calculations of correlations that influence vertical electron current through semiconductor and stacked van der Waals heterostructures. The forward physical model in our study considers a single band in the tight-binding Hamiltonian and, in doing so, avoids the computational burden of more sophisticated approaches such as density functional theory (DFT) or alternative methods used for studying electronic structure [39,40]. Green’s function methods have previously been used alongside DFT to study electron transport in devices [41–43], and the framework of DFT has recently been used to study complex band structure [44,45]. The connection between tight-binding and DFT calculations [46–50] has also been studied.

It is also worth noting that while the optimal design of electron transport in novel tunable materials such as van der Waals superatomic semiconductors [51,52] may benefit from our methodology, the forward solution might require a significantly more computationally intensive and sophisticated physical model.

6. Conclusion

A tight-binding model of electron transport on a 1D lattice has been developed and used to find optimal current–voltage characteristics in which electrons are transmitted through a multi-layer heterostructure. Potential applications of this approach to combining a physical model of electron transport with optimal parameter exploration include the study of vertical electron transport through van der Waals stacked few-layer quantum materials and nano-scale single-crystal semiconductor heterostructures.

The physics that the optimization algorithm exploits to explore the non-convex and non-intuitive design space may be understood as electron velocity mismatch between layers and the resulting spectrum of broad transmission resonances that vary as a function of onsite potential, U , and applied voltage bias, V_{bias} . The number of resonances in the open system is a resource that increases with number of layers, N_b . Additionally, the next-nearest-neighbor hopping term, t_2 , can control the spectral density of resonances, including those at large values of k in the related bulk complex band structure.

CRediT authorship contribution statement

Walter Unglaub: Writing – original draft, Visualization, Software, Investigation, Formal analysis, Data curation. **A.F.J. Levi:** Writing – review & editing, Writing – original draft, Methodology, Formal analysis, Data curation, Conceptualization.

Declaration of competing interest

The authors declare that they have no known competing financial interests or personal relationships that could have appeared to influence the work reported in this paper.

Data availability

Data will be made available on request.

References

- [1] K. Kinoshita, R. Moriya, S. Okazaki, Y. Zhang, S. Masubuchi, K. Watanabe, T. Taniguchi, T. Sasagawa, T. Machida, Resonant tunneling between quantized subbands in van der Waals double quantum well structure based on few-layer WSe_2 , *Nano Lett.* 22 (2022) 4640–4645.
- [2] P.K. Srivastava, Y. Hassan, D.J.P. de Sousa, Y. Gebredingle, M. Joe, F. Ali, Y. Zheng, W.J. Yoo, S. Ghosh, J.T. Teherani, B. Singh, T. Low, C. Lee, Resonant tunnelling diodes based on twisted black phosphorus homostructures, *Nat. Electron.* 4 (2021) 269–276.
- [3] S.-J. Liang, B. Cheng, X. Cui, F. Miao, Van der Waals heterostructures for high-performance device applications: Challenges and opportunities, *Adv. Mater. Primers* 32 (2020) 1903800.
- [4] A. Castellanos-Gomez, X. Duan, Z. Fei, H.R. Gutierrez, Y. Huang, X. Huang, J. Quereda, Q. Qian, E. Sutter, P. Sutter, Van der Waals heterostructures, *Nat. Rev. Methods Primers* 2 (2022) 58.
- [5] E. Sasoglu, I. Mertig, Theoretical prediction of semiconductor-free negative differential resistance tunnel diodes with high peak-to-valley current ratios based on two-dimensional cold metals, *ACS Appl. Nano Mater.* 6 (2023) 3758–3766.
- [6] Y. Mao, Z. Huang, Electron transport properties of van der Waals heterostructures composed by one-dimensional carbon nanotubes and two-dimensional germanium selenide, *Results Phys.* 52 (2023) 106835.
- [7] V. Ryzhii, T. Otsuji, M. Ryzhii, V.Ya. Aleshkin, A.A. Dubinov, V. Mitin, M.S. Shur, Vertical electron transport in van der Waals heterostructures with graphene layers, *J. Appl. Phys.* 117 (2015) 154504.
- [8] Q. Qian, Z. Wan, X. Duan, Van der Waals integration of artificial heterostructures and high-order superlattices, *Natl. Sci. Open Primers* 2 (2023) 20220034.
- [9] E.E. Vdovin, A. Mishchenko, M.T. Greenaway, M.J. Zhu, D. Ghazaryan, A. Misra, Y. Cao, S.V. Morozov, O. Makarovskiy, T.M. Fromhold, A. Patane, G.J. Slotman, M.I. Katsnelson, A.K. Geim, K.S. Novoselov, L. Eaves, Phonon-assisted resonant tunneling of electrons in graphene-boron nitride transistors, *Phys. Rev. Lett.* 116 (2016) 186603.
- [10] L. Wang, S. Papadopoulos, F. Iyikanat, J. Zhang, J. Huang, T. Taniguchi, K. Watanabe, M. Calame, M.L. Perrin, F.J. Garcia de Abajo, L. Novotny, Exciton-assisted electron tunneling in van der Waals heterostructures, *Nature Mater.* 22 (2023) 1094–1099.
- [11] K.C. Magruder, A.F.J. Levi, Optimal design of a semiconductor heterostructure tunnel diode with nonlinear current–voltage characteristic, *Physica E* 44 (2012) 1503–1509.
- [12] F. Bloch, Über die quantenmechanik der elektronen in kristallgittern, *Z. Phys.* 52 (1929) 555–600.
- [13] J.C. Slater, G.F. Koster, Simplified LCAO method for the periodic potential problem, *Phys. Rev.* 94 (1954) 1498–1524.
- [14] V. Heine, On the general theory of surface states and scattering of electrons in solids, *Proc. Phys. Soc.* 81 (1963) 300.
- [15] Y. Chang, J.N. Schulman, Complex band structures of crystalline solids: An eigenvalue method, *Phys. Rev. B* 25 (1982) 3975–3986.
- [16] J.N. Schulman, Y. Chang, Reduced Hamiltonian method for solving the tight-binding model of interfaces, *Phys. Rev. B* 27 (1983) 2346–2354.
- [17] D.J. Chadi, M.L. Cohen, Tight-Binding Calculations of the Valence Bands of Diamond and Zincblende Crystals, LBNL, 1974.
- [18] D.A. Papaconstantopoulos, *Handbook of the Band Structure of Elemental Solids*, Springer, New York, NY, 1986.
- [19] P. Vogl, H.P. Hjalmarson, J.D. Dow, A semi-empirical tight-binding theory of the electronic structure of semiconductors, *J. Phys. Chem. Solids* 44 (1983) 365–378.
- [20] P.A. Cox, *The Electronic Structure and Chemistry of Solids*, Oxford University Press, 1987.
- [21] E.N. Economou, *Green's Functions in Quantum Physics*, Springer-Verlag Berlin Heidelberg, 2006.
- [22] I.A. Veres, T. Berer, O. Matsuda, Complex band structures of two dimensional phononic crystals: Analysis by the finite element method, *J. Appl. Phys.* 114 (2013) 083519.
- [23] M.G. Reuter, *A Unified Perspective of Complex Band Structure: Interpretations, Formulations, and Applications*, Vol. 29, IOP Publishing, 2016, 053001.
- [24] J.M. Ziman, *Principles of the Theory of Solids*, Cambridge University Press, 1972.
- [25] S. Datta, *Electronic Transport in Mesoscopic Systems*, Cambridge University Press, 1995.
- [26] H.M. Pastawski, E. Medina, 'Tight binding' methods in quantum transport through molecules and small devices: From the coherent to the decoherent description, *Rev. Mex. Fis.* 47S1 (2001) 1–23.
- [27] M. Kollar, M. Eckstein, K. Byczuk, N. Blümer, P. van Dongen, M.H. Radke de Cuba, W. Metzner, D. Tanasković, V. Dobrosavljević, G. Kotliar, D. Vollhardt, Green functions for nearest- and next-nearest-neighbor hopping on the Bethe lattice, *Ann. Phys., Lpz.* 517 (2005) 642–657.
- [28] M. Luisier, A. Schenk, W. Fichtner, G. Klimeck, Atomistic simulation of nanowires in the $sp^3d^5s^*$ tight-binding formalism: From boundary conditions to strain calculations, *Phys. Rev. B* 74 (2006) 205323.
- [29] J.A. Lawlor, M.S. Ferreira, Green functions of graphene: An analytic approach, *Physica B* 463 (2015) 48–53.
- [30] A. Komnik, S. Heinze, Analytical results for the green's functions of lattice fermions, *Phys. Rev. B* 96 (2017) 155103.
- [31] E. Kogan, G. Gumbs, Green's functions and DOS for some 2D lattices, *Graphene* 10 (2021) 1–12.
- [32] M. Alvarado, A.L. Yeyati, 2D topological matter from a boundary green's functions perspective: Faddeev-LeVerrier algorithm implementation, *SciPost Phys.* 13 (2022) 009.
- [33] A. Alase, E. Cobanera, G. Ortiz, L. Viola, Generalization of Bloch's theorem for arbitrary boundary conditions: Theory, *Phys. Rev. B* 96 (2017) 195133.
- [34] E. Cobanera, A. Alase, G. Ortiz, L. Viola, Generalization of Bloch's theorem for arbitrary boundary conditions: Interfaces and topological surface band structure, *Phys. Rev. B* 98 (2018) 245423.
- [35] A.F.J. Levi, G. Rosen, A novel formulation of the adjoint method in the design of quantum electronic devices, *SIAM J. Control Optim.* 48 (2010) 3191–3223.
- [36] N.F. Hinsche, M. Fechner, P. Bose, S. Ostanin, J. Henk, I. Mertig, P. Zahn, Strong influence of complex band structure on tunneling electroresistance: A combined model and ab initio study, *Phys. Rev. B* 82 (2010) 214110.
- [37] N.G. Einspruch, W.R. Frensley (Eds.), *Heterostructures and Quantum Devices*, Academic Press, San Diego, California, 1994, Chapter 9.
- [38] The idea that accessing different states in complex band structure can be used as a guide to explain electron transport in nano-scale structures has been explored previously in the context of electron wave packet tunneling by, W. Unglaub, A.F.J. Levi, Wave packet tunneling and imaginary wave vector dispersion, *Phys. Open* 17 (2023) 100164.
- [39] R. Haydock, V. Heine, M.J. Kelly, Electronic structure based on the local atomic environment for tight-binding bands, *J. Phys. C: Solid State Phys.* 5 (1972) 2845.
- [40] R. Haydock, V. Heine, M.J. Kelly, Electronic structure based on the local atomic environment for tight-binding bands. II, *J. Phys. C: Solid State Phys.* 8 (1975) 2591.
- [41] J. Taylor, H. Guo, J. Wang, Ab initio modeling of quantum transport properties of molecular electronic devices, *Phys. Rev. B* 63 (2001) 245407.
- [42] M. Brandbyge, J. Mozos, P. Ordejón, J. Taylor, K. Stokbro, Density-functional method for nonequilibrium electron transport, *Phys. Rev. B* 65 (2002) 165401.
- [43] K. Stokbro, First-principles modeling of electron transport, *J. Phys.: Condens. Matter.* 20 (2008) 064216.
- [44] S. Tsukamoto, T. Ono, S. Iwase, S. Blügel, Complex band structure calculations based on the overbridging boundary matching method without using green's functions, *Phys. Rev. B* 98 (2018) 195422.
- [45] E. Bosoni, S. Sanvito, Complex band structure with non-orthogonal basis set: analytical properties and implementation in the SIESTA code, *J. Phys.: Condens. Matter.* 34 (2021) 105501.
- [46] A.P. Sutton, M.W. Finnis, D.G. Pettifor, Y. Ohta, The tight-binding bond model, *J. Phys. C: Solid State Phys.* 21 (1988) 35.
- [47] D. Porezag, Th. Frauenheim, Th. Köhler, G. Seifert, R. Kaschner, Construction of tight-binding-like potentials on the basis of density-functional theory: Application to carbon, *Phys. Rev. B* 51 (1995) 12947–12957.
- [48] A. Pecchia, G. Penazzi, L. Salvucci, A. Di Carlo, Non-equilibrium green's functions in density functional tight binding: method and applications, *New J. Phys.* 10 (2008) 065022.
- [49] R.M. Martin, *Electronic Structure: Basic Theory and Practical Methods*, Cambridge University Press, 2004.
- [50] C.A. Broderick, E.P. O'Reilly, S. Schulz, Perspective: Theory and simulation of highly mismatched semiconductor alloys using the tight-binding method, *J. Appl. Phys.* 135 (2024) 100902.
- [51] E.A. Doud, A. Voevodin, T.J. Hochuli, A.M. Champsaur, C. Nuckolls, X. Roy, Superatoms in materials science, *Nat. Rev. Mater.* 5 (2020) 371–387.
- [52] J.M. Baxter, C.S. Koay, D. Xu, S.-W. Cheng, J.A. Tulyagankhodjaev, P. Shih, X. Roy, M. Delor, Coexistence of incoherent and ultrafast coherent exciton transport in a two-dimensional superatomic semiconductor, *J. Phys. Chem. Lett.* 14 (2023) 10249–10256.